

Chapter 6:  
Relating Surface-atmosphere Exchange to Remotely  
Sensed Quantities

**Chapter Contents**

<b>6.1</b>	<b>Introduction .....</b>	<b>205</b>
<b>6.2</b>	<b>Remotely Sensed Data .....</b>	<b>208</b>
6.2.1	Calculation of <i>NDVI</i> .....	208
6.2.2	<i>NDVI</i> of the OASIS Domain .....	210
<b>6.3</b>	<b>Description of the Source-area Model .....</b>	<b>213</b>
6.3.1	General .....	213
6.3.2	Source Area Model.....	213
6.3.3	Application to Ground-based and Aircraft Observations .....	215
<b>6.4</b>	<b>Source-area Weighted <i>NDVI</i> .....</b>	<b>218</b>
6.4.1	Ground-based Sites .....	218
6.4.2	Aircraft Grid Pattern.....	220
6.4.3	Aircraft Transect .....	221
<b>6.5</b>	<b>Surface Properties and <i>NDVI</i> .....</b>	<b>224</b>
6.5.1	Ground-based Sites .....	224
6.5.2	Synthesis of Ground-based and Aircraft Data.....	226
6.5.3	Extension of Point Observations to OASIS Domain.....	229
<b>6.6</b>	<b>Summary and Conclusions .....</b>	<b>232</b>
<b>6.7</b>	<b>Appendix: Source-area Model.....</b>	<b>235</b>
6.7.1	Equation Set .....	235
6.7.2	Numerical Method.....	238
6.7.3	Source-area Example.....	240

## 6.1 Introduction

Previous attempts to relate remotely sensed quantities to surface-atmosphere exchange have followed one of two methods.

First, direct relationships between a vegetation index (VI) and the fluxes of H<sub>2</sub>O and CO<sub>2</sub> have been examined (Cihlar et al. 1992; Desjardins et al., 1992a; Chen et al. 1999a; McMichael et al., 1999). These comparisons show considerable scatter and the empirical relationships derived from them are expected to be both site and time specific. It is likely that much of the scatter arises because the VI is essentially a property of the surface, responding to the type and health of the vegetation, whereas  $F_E$  and  $F_C$  are controlled by both surface type and meteorology via the stomatal and aerodynamic conductances. A development of this direct approach is to compare values of the VI and  $F_C$  integrated over some time period, usually around 14 days (Wylie et al., 2003). These comparisons show less scatter compared to those using hourly values because the effect of synoptic conditions on  $F_C$  is reduced by integrating over time periods longer than the synoptic cycle. However, even though the scatter is reduced, the resulting relationships are still site and time specific and this limits their application outside the conditions under which they were derived.

The second approach is the integration of remotely sensed data with biosphere models using two general techniques, "forcing" and "recalibration" (Moulin et al., 1998; Oliosio et al., 1999). The "forcing" technique involves estimating input parameters required by the model from remotely sensed data, the most common of these being leaf area index ( $L_{ai}$ ) and the fraction of photosynthetically active radiation absorbed by the vegetation ( $fPAR$ ). Considerable progress has been made recently in the operational extraction of these quantities from the Moderate-resolution Imaging Spectrometer (MODIS) on board the Earth Observing System (EOS) Terra satellites (Huete et al., 2002; Myneni et al., 2002). However, there remain problems associated with saturation (Gitelson et al., 2003), the distribution of chlorophyll through the canopy (Dawson et al., 2003) and gaps in the time series of values due to cloud cover at the time of the satellite pass. In an alternative scheme, Braun et al. (2001) use precipitation data from weather radars and cloud cover from

the METEOSAT satellite to constrain the output from a mesoscale model that provides the meteorological input to a Soil-Vegetation-Atmosphere Transfer (SVAT) model. Mahrt et al. (1998) explore a more direct method by relating the evaporative fraction to the radiative surface temperature, the Normalised Difference Vegetation Index (*NDVI*), the air temperature and, to account for shading effects, the solar zenith angle. They find that a multi-variable model performs well in predicting  $\alpha_E$  for forest and agricultural land-uses.

The "recalibration" technique involves the adjustment of one or more model parameters to minimise the difference between a model output and the same quantity estimated from remotely sensed data. Most of the work in this area has concentrated on matching the surface temperature from the model to the brightness temperature calculated from remotely sensed data (Oliosio et al., 1999; Flerchinger et al., 1998) by tuning the soil moisture or related quantities in the model. Zhan and Kustas (2001) extend this approach to calculate both  $F_E$  and  $F_C$  using remotely sensed observations of the radiometric surface temperature to avoid the need for measurements of the surface soil water content. Other variations to the "recalibration" approach involve using plots of VI versus surface temperature to estimate soil moisture (Carlson et al., 1995), fractional vegetation cover and surface energy fluxes (Gillies et al., 1997), the Priestly-Taylor coefficient (Jiang and Islam, 2001) and the evaporative fraction (Nishida et al., 2003).

This chapter examines a new approach to the forcing method that integrates observations and remotely sensed data to provide estimates of surface properties applicable to regions of the order of 100 km square. The rationale for this approach is that surface properties are less sensitive to meteorological conditions than the surface fluxes and as a result they are expected to show greater correlation with remotely sensed quantities. A robust relationship between a surface property and a remotely sensed quantity allows measurements of the surface property at a small number of locations to be interpolated across a wider area. The interpolated values of the surface properties can then be input, with the appropriate meteorology, to a model that calculates the regional scale fluxes of heat, water vapour and carbon dioxide.

To this end, the relationships between the Normalised Difference Vegetation Index ( $NDVI$ ) and the surface properties  $\alpha_E$ ,  $g_{sx}$ ,  $\beta$  and  $W_{UE}$  are tested and subsequently used to derive maps of the surface properties over the OASIS domain. The first step in this process is to match the observations of the surface properties to the  $NDVI$  image so that the relationship between these quantities can be examined. The matching is done using a source-area model that calculates the relative weighting of elements across the surface patch responsible for contributing 80% of the observed flux. These weights are then applied to the  $NDVI$  image to produce a source-area weighted  $NDVI$  value for each ground-based or aircraft observation. Averages over all available data are then used to derive empirical relationships between the surface properties and the source-area weighted  $NDVI$ .

This work has some similarities with that described in Cihlar et al. (1992) and Chen et al. (1999a). Cihlar et al. (1992) use data from the Advanced Very High Resolution Radiometer (AVHRR) sensor on the NOAA-series of satellites and a simple source-area model to calculate a source-area weighted  $NDVI$  which they then compare to aircraft observations of  $F_C$ . Chen et al. (1999a) use a source-area model with a land-cover map derived from Landsat Thematic Mapper (TM) image to separate aircraft observations of  $F_C$  into contributions from eight major land-cover types. These approaches rely on direct relationships between remotely sensed quantities and the flux of  $CO_2$ . The approach adopted here is distinct from this because it considers the relationship between remotely sensed data and surface properties and extends the analysis to include water vapour.

Section 6.2 describes the calculation of  $NDVI$  from the Landsat 5 TM data and the use of  $NDVI$  as an indicator of surface heterogeneity across the OASIS domain. The source-area model is outlined in Section 6.3 and its application to the ground-based and aircraft data is discussed. Section 6.4 presents the results obtained by applying the source-area model to the  $NDVI$  image using the ground-based and aircraft data and discusses the spatial variability in the source-area weighted  $NDVI$ . The relationships between the surface properties and  $NDVI$  are examined in Section 6.5 and used to extend the observations of the surface properties to the OASIS domain. Conclusions are presented in Section 6.6.

## 6.2 Remotely Sensed Data

### 6.2.1 Calculation of *NDVI*

Calculation of *NDVI* from the Landsat 5 TM data requires conversion of the radiometer outputs to spectral radiance, conversion of the spectral radiance to spectral reflectance and calculation of *NDVI* from the spectral reflectance. No atmospheric correction has been applied to the calculated radiance values but vegetation indices formed from the ratio of reflectances are insensitive to this correction.

The Australian Centre for Remote Sensing (ACRES) supply the Landsat 5 TM image data as byte values for each pixel in each spectral band and these need to be converted to reflectance before the *NDVI* can be calculated. Simple vegetation indices (VI) can be calculated from remotely sensed data without converting the byte values to reflectance but these are not directly comparable across sensors or from one image to another from the same sensor. As a result, any relationship derived between them and surface-atmosphere exchange will be specific to the radiometer used and the sun-target-radiometer geometry of the image. Correct calibration of the image means that data from different platforms collected at different times of the day can be compared.

The calibration model used to convert the radiometer output to spectral reflectance comes from Arino et al. (1994). These authors propose a linear relationship between the byte value of the radiometer output and the spectral radiance in each band of the Landsat 5 TM sensor:

$$L(\lambda) = a_1(\lambda)Q_{cal}(\lambda) + a_0(\lambda) \quad 6.1$$

where  $L(\lambda)$  is the spectral radiance in  $\text{W m}^{-2} \text{sr}^{-1} \mu\text{m}^{-1}$  and  $Q_{cal}(\lambda)$  is the byte value for each pixel after relative calibration. The spectral radiance calculated using Equation 6.1 is independent of the measurement platform but is still dependent on the time of the satellite pass. This dependence is removed by converting the radiance to reflectance using:

$$\rho(\lambda) = \frac{\pi L(\lambda)}{d^2 E_s(\lambda) \cos \Theta} \quad 6.2$$

where  $\rho(\lambda)$  is the spectral reflectance,  $E_s(\lambda)$  is the solar radiance in each band,  $\Theta$  is the solar zenith angle and  $d$  is the ratio of the mean to actual Sun-Earth distance given by:

$$d = \frac{1}{(1 - 0.016729 \cos(0.9856(DOY - 4)))}. \quad 6.3$$

$DOY$  in Equation 6.3 is the day of the year. Table 6.1 lists the values for  $a_1$ ,  $a_0$  and the solar radiance in each band given by Arino et al. (1994).

**Table 6.1** Offset and gain coefficients and solar radiance for bands 1 to 5 and 7 of the Landsat 5 Thematic Mapper.

Band	1	2	3	4	5	7
$a_0$	-1.5	-3.1	-2.7	-2.5	-0.45	-0.3
$a_1$	0.731	1.353	0.971	1.069	0.143	0.076
$E_s(\lambda) \text{ W m}^{-2} \mu\text{m}^{-1}$	1957	1829	1557	1047	219.3	74.52

The  $NDVI$  is then calculated from the spectral reflectance for bands 3 and 4 as:

$$NDVI = \frac{\rho(4) - \rho(3)}{\rho(4) + \rho(3)} \quad 6.4$$

The  $NDVI$  calculated using the above model will be independent of the radiometer and the time of the satellite pass and as such, it should be comparable with  $NDVI$  derived from other platforms. However, this model leads to negative values of  $NDVI$  for pixels that are dominated by open water. The Landsat 5 TM image of the OASIS domain contains many bodies of open water including Lake Urana, the Murrumbidgee River and numerous small dams. The negative  $NDVI$  values associated with these features have been set to zero and the implications of this are discussed later in this chapter.

### 6.2.2 NDVI of the OASIS Domain

The *NDVI* image for the OASIS domain calculated using data from the Landsat 5 pass on 8 October 1995 is shown in Figure 6.1.

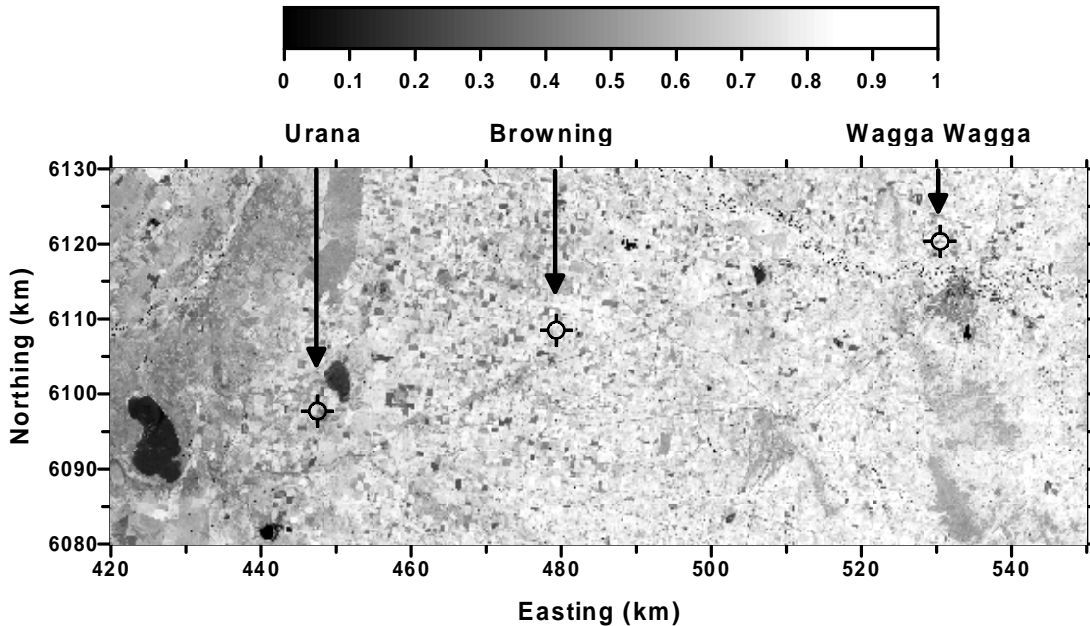


**Figure 6.1** *NDVI* image for the OASIS domain on 8 October 1995. The crossed circles show the location of the ground-based sites.

The major features of the OASIS domain are clearly identified in the *NDVI* image. The Murrumbidgee River appears as a line of black dots across the top right corner of the image with the city of Wagga Wagga as the dark grey area beneath it. Lakes Cullival and Urana appear as the black areas in the bottom left corner of the image. The light grey shading indicates areas of remnant native vegetation. There is a clear gradient in *NDVI* from values of 0.5 (mid grey) at the western end of the domain to 0.8 (white) at the eastern end. The image also shows that there are many length scales evident in the surface cover, for example the regional scale changes in vegetation type (remnant native vegetation in the west to mixed agricultural in the east) and the decreasing field size from west to east.

One of the aims of the OASIS experiment was to characterise the regional scale fluxes of heat, water vapour and  $\text{CO}_2$  using a network of ground-based measurement sites. The success of this aim depends on the extent to which the ground-based sites are representative of the larger region and this can be tested using *NDVI*. Several

authors (Cihlar et al., 1992; Desjardins et al., 1992a; McMichael et al., 1999) have noted a close relationship between *NDVI* and the fluxes of water vapour and CO<sub>2</sub>. This allows *NDVI*, which is available at high spatial resolution from satellite images, to be used as a surrogate for the fluxes in assessing the degree to which the ground-based sites are representative of their surroundings. Further evidence for this association is presented later in this chapter.

Figure 6.2 shows a histogram of *NDVI* values over the whole of the OASIS domain with the *NDVI* values for the ground-based sites marked by arrows. The method for determining the *NDVI* values of the ground-based sites is explained in the next section. The ground-based sites have *NDVI* values that are representative of the middle and upper range of values in the image of the whole domain; areas with the lowest *NDVI* values have not been sampled. Pixels with an *NDVI* less than that of the Urana pasture site comprise approximately 18% of the image area and heat and water vapour fluxes over these areas are not represented by the available ground-based measurements. CO<sub>2</sub> flux measurements were only made at Wagga and Browning during 1995 and approximately 40% of the OASIS domain had an *NDVI* less than the value for the Browning pasture site.

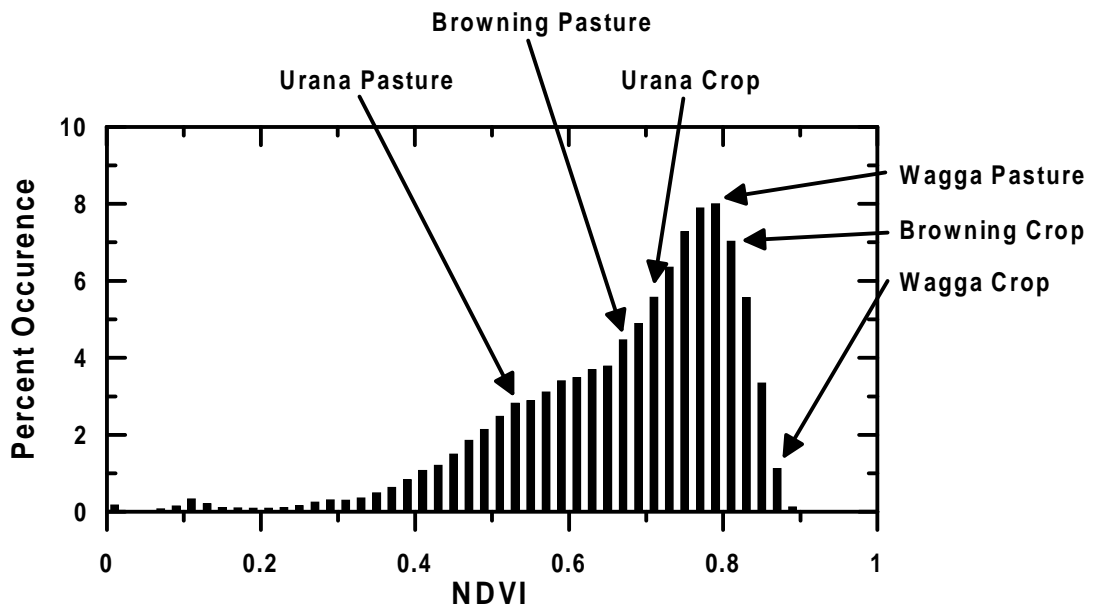


**Figure 6.2** Histogram of *NDVI* values for the OASIS domain.

## Chapter Six

The increase in  $NDVI$  from the west to east matches the change in  $\alpha_E$ ,  $g_{sx}$ ,  $\beta$  and  $W_{UE}$  described in Chapter Five. This suggests that there may be a useful relationship between  $NDVI$  and these surface properties. Before such a relationship can be investigated, it is necessary to establish the  $NDVI$  of the source-area at the surface that makes the majority, say 80%, of the contribution to the measured flux. In the case of the ground-based sites, whose locations were chosen to give adequate fetch over the fields in which they were sited, simply averaging the  $NDVI$  over the field containing the tower may provide a reasonable approximation to the source-area  $NDVI$ . The aircraft observations can not be treated as simply because the aircraft passes over many surface types and is influenced by a greater upwind surface area due to its greater measurement height. The link between observations of the flux of heat, water vapour and  $CO_2$  and the surface area contributing to these observations can be made using a model of the source-area, often called the measurement footprint (Schuepp et al., 1990). Once the contribution, or weight, of each element of the source-area has been calculated, this weighting function can be overlaid on the  $NDVI$  image and the weighted-average  $NDVI$  of the source-area calculated. The following section describes the source-area weight model used in the current work.

## **6.3 Description of the Source-area Model**

### **6.3.1 General**

Source-area models seek to estimate the upwind surface area that contributes to an observation. The extent of this source-area depends on the measurement height, the surface roughness and the meteorology. There are two approaches to estimating the source-area, both of which are based on modelling the diffusion of a passive scalar in the atmospheric boundary layer. The first uses an approximate analytical solution to the 2-dimensional advection-diffusion equation originally derived for neutral conditions (Horst and Weil, 1992) and later extended, in contradiction to the original premise, to unstable conditions (Horst and Weil, 1995). Subsequent experimental verification by Finn et al. (1996) and Leclerc et al. (2003) proved the utility of this extension. The second approach is applicable to measurements made in the surface- and mixed-layers and uses Lagrangian particle dispersion. The advantage of this approach is its ability to treat cases where the measurement height is above the surface-layer but this comes at the cost of greater complexity and computational overhead. Comparison of the source-area results from the analytical and Lagrangian methods shows that they give similar results when the measurement height is just above the surface layer in unstable conditions (Kljun et al., 2003; Leclerc et al., 2003). For this reason, and because of its low computational overhead, the analytical method has been used for the current work.

### **6.3.2 Source Area Model**

The source-area model used here is based on the formulations presented in Horst and Weil (1992, 1994 and 1995) and the relevant equations are given in the Appendix at the end of this chapter. The underlying assumptions of this model are that the measured flux can be treated as the sum of contributions from point sources at the surface and that the vertical transport is analogous to the upward diffusion of a passive scalar released at the surface. Horst and Weil (1992) demonstrate that the dependence of the source-area weight on crosswind location is the same as the crosswind concentration from a point source at the surface. In combination with the

basic assumptions, this allows the source-area weight function to be calculated using established equations for estimating diffusion from a point source at the surface. Good agreement between the model and experimental results has been demonstrated by Finn et al. (1996).

The crosswind integrated source-area weight function,  $\bar{f}^y$ , and the cumulative sum of  $\bar{f}^y$  are shown in Figure 6.3 for unstable conditions with measurement heights of 4.5 and 20 m, representative of the ground-based and aircraft observations respectively. The crosswind integrated source-area weight for observations at 4.5 m rises sharply to a peak at 34 m upwind of the tower and drops rapidly as the upwind distance increases. For observations at 20 m, the maximum value of the source-area weight function is a factor of four smaller and occurs at an upwind distance of 135 m. The effect of measurement height is also evident in the plot of  $\sum \bar{f}^y$ . This shows that 80% of the flux comes from an upwind distance of less than 240 m for  $z = 4.5$  m compared to 770 m for  $z = 20$  m.

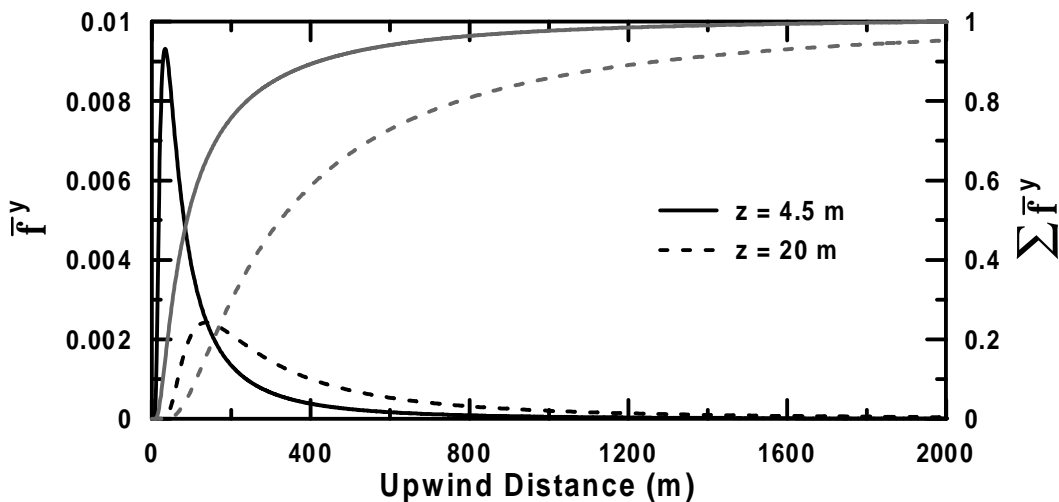


**Figure 6.3** Cross-wind integrated source-area weight function  $\bar{f}^y$  (black) and the cumulative cross-wind integrated source-area weight function  $\sum \bar{f}^y$  (grey) as functions of upwind distance for measurement heights of 4.5 m (solid) and 20 m (dotted). Parameters for both plots were  $L = -30$  m,  $u_* = 0.5$  m s<sup>-1</sup>,  $\sigma_{WD} = 20^\circ$  and  $z_0 = 0.03$  m.

Figure 6.4a and b show isopleths enclosing the surface areas that contribute 20, 50 and 80% of the flux observed at 4.5 and 20 m respectively for the same conditions as

used in Figure 6.3. The upwind extent of the 80% isopleth for  $z = 20$  m is four times greater than that for  $z = 4.5$  m and the crosswind extent is three times greater. The area enclosed by the 80% isopleth for  $z = 20$  m is approximately  $216,000 \text{ m}^2$  compared to  $18,000 \text{ m}^2$  for  $z = 4.5$  m.

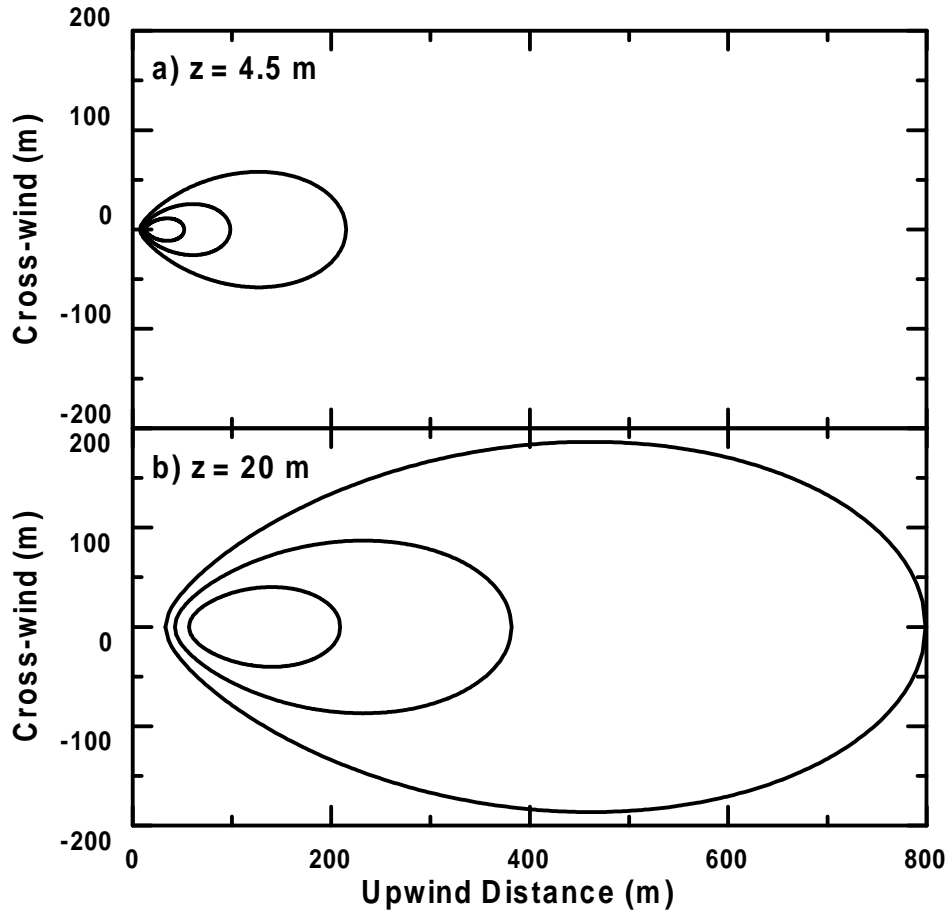


**Figure 6.4** Isopleths of 80% (outer), 50% (middle) and 20% (inner) contribution to the flux measured at a) 4.5 m and b) 20 m. Parameters as in Figure 6.3.

### 6.3.3 Application to Ground-based and Aircraft Observations

The source-area weighted *NDVI* was calculated by multiplying the *NDVI* at each upwind location by the value of the crosswind integrated source-area weight function at that location, summing the weighted *NDVI* values and normalising the sum by the sum of the weights. The method is defined in Equation 6.5 and illustrated in Figure 6.5.

$$NDVI_{SAW} = \frac{\sum_i \bar{f}^y(x_i, z) NDVI(x_i)}{\sum_i \bar{f}^y(x_i, z)} \quad 6.5$$

The crosswind integrated source-area weight function is used instead of the three-dimensional source-area weight function,  $f(x_i, y_j, z)$ , to reduce the computational overhead. The number of calculations required by the three-dimensional method is proportional to  $N^2$  where  $N$  is the number of points at which the source-area weight function is calculated. By comparison, the number of calculations required for the crosswind integrated method is proportional to  $N$ . The error introduced by this approximation was checked by comparing the source-area weighted  $NDVI$  calculated using both  $\bar{f}^y$  and  $f(x_i, y_j, z)$  with a subset of the data and no significant differences were found.

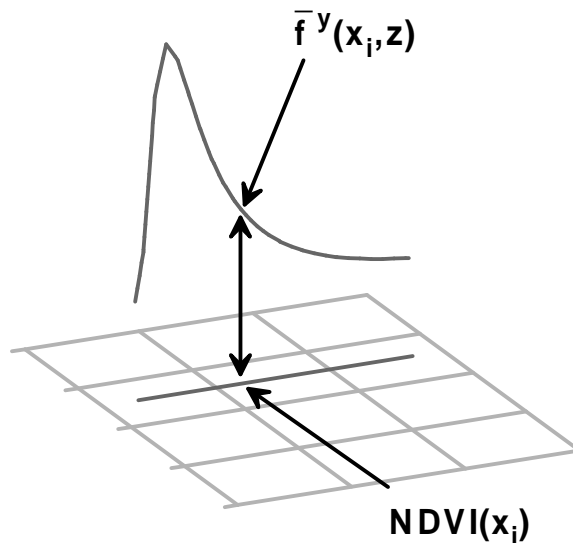


**Figure 6.5** Schematic diagram showing the method for calculating the source-area weighted  $NDVI$  using the crosswind integrated source-area weight function.

Values of the source-area weighted  $NDVI$  were calculated for each ground- or aircraft-based observation and then averaged over all available data. In the case of the ground-based observations, the wind direction for each observing period was used to orient  $\bar{f}^y$  into the wind, resulting in a star-like pattern centred on the tower

## Relating Surface-atmosphere Exchange to Remotely Sensed Quantities

location with each radial arm of the star yielding a single source-area weighted value of  $NDVI$ . These individual values were then averaged to produce the final source-area weighted  $NDVI$  for each site.

The process for the aircraft observations was somewhat different because the fluxes measured by the aircraft are averaged along segments of the flight track, not at a single location as for the ground-based sites. For the aircraft transect data,  $\bar{f}^y$  was calculated every 1 km along each 10 km flight segment, using the average fluxes and wind direction for the whole segment, and the resulting source-area weighted  $NDVI$  were then averaged to provide a single value for the segment. For the aircraft grid data,  $\bar{f}^y$  was calculated every 500 m along each 2 km grid segment. This is an approximation to the real case for two reasons. First, the local conditions determine the upwind surface area influencing the aircraft observations at a given location and not the average along a segment of the flight track. Second, the  $NDVI$  of the surface contributing to the flux measurements is estimated by averaging eleven (transect) or five (grid) values spaced along the flight segments. The surface areas between these will have influenced the flux measurements but they are not included in the source-area weighted  $NDVI$ . The effect of the second approximation was checked by decreasing the spacing between points where  $\bar{f}^y$  was calculated to 250 m but this did not alter the results. The effect of the first approximation is expected to be small.

These averaging processes are illustrated in the following section.

## 6.4 Source-area Weighted *NDVI*

### 6.4.1 Ground-based Sites

Figure 6.6 shows plots of the crosswind integrated source-area weight function overlaid on the *NDVI* images for the crop and pasture sites at Wagga, Browning and Urana. Crop fields appear as light grey, pasture fields at the same location are mid to dark grey, fallow areas appear as dark grey and water bodies are black. The  $\overline{f}^y$  for each observation period is plotted as a bold line originating at the tower location and oriented into the wind. The lines are truncated at 80% of the contribution to the flux and their length is determined mainly by the measurement height (2.5 m for Wagga and Urana and 4.5 m for Browning) and the stability,  $z/L$ . Lower measurement heights and increasing instability (larger  $F_H$ , smaller  $u_*$ ) limit the extent of the upwind area that influences an observation.

The *NDVI* of the crop fields is higher than the *NDVI* of the pastures at each of the ground-based sites and the *NDVI* shows a general decrease from Wagga to Urana. Some of the source-area weight lines at the Wagga and Browning crop and pasture sites and the Urana crop site extend outside the field containing the tower and only lie completely within the field for the Urana pasture site. This means that flux measurements made at the Wagga and Browning crop and pasture sites and the Urana crop site will include contributions from surface areas outside the fields containing the towers. However, the effect will be small because the source-area weight function peaks close to the tower for low measurement heights. The source-area weighted *NDVI* values for the ground-based sites are given in Table 6.2. There is a significant range of *NDVI* values at each of the ground-based sites.

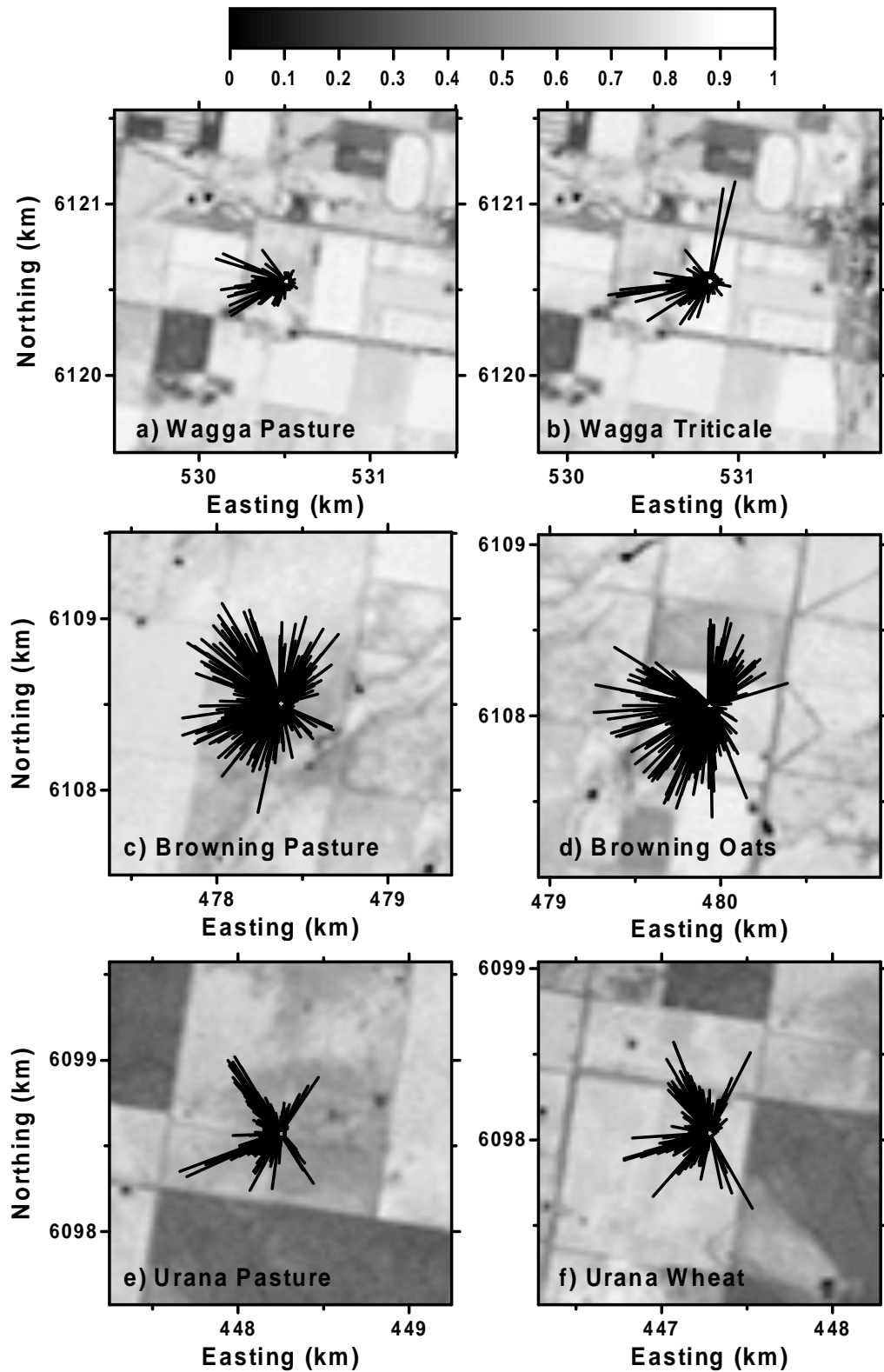


**Figure 6.6** *NDVI* images of a) Wagga pasture, b) Wagga triticale, c) Browning pasture, d) Browning oats, e) Urana pasture and f) Urana wheat fields during October 1995. Overlaid lines mark the upwind extent of the source-area contributing 80% of the turbulent fluxes.

**Table 6.2** Source-area weighted *NDVI* values for the ground-based sites.

<i>NDVI</i>	Mean	SD	Max	Min
Wagga Triticale	0.86	0.01	0.87	0.81
Wagga Pasture	0.77	0.04	0.84	0.70
Browning Oats	0.80	0.01	0.82	0.75
Browning Pasture	0.67	0.02	0.72	0.62
Cooinda Canola	0.75	0.03	0.79	0.67
Wattles Wheat	0.82	0.01	0.84	0.75
Urana Wheat	0.70	0.02	0.73	0.67
Urana Pasture	0.53	0.02	0.59	0.50

#### 6.4.2 Aircraft Grid Pattern

Figure 6.7 shows a plot of  $\overline{f^y}$  for the aircraft grid flights at 20 m overlaid on the *NDVI* image of the grid area and a contour plot of the corresponding source-area weighted *NDVI* for the grid area. The locations of the Wattles wheat (WW), Browning oats (BO), Browning pasture (BP) and Cooinda canola (CC) ground-based sites are marked as indicated. The upwind extent of  $\overline{f^y}$  has been calculated using aircraft observations of fluxes averaged over 2000 m. The use of this short averaging length represents a compromise between the desire to resolve small-scale surface features and the need to include the most important wavelengths in the flux estimates. The short averaging length will result in underestimation of approximately 10% for both scalar and momentum fluxes (Kaimal and Finnigan, 1994). This will lead to values of  $L$  that are 20% smaller in magnitude (ie more unstable) but this is not expected to have a significant impact on the location of the peak in  $\overline{f^y}$  or on the upwind extent of the 80% cut-off.

The *NDVI* image clearly shows the mosaic of land uses over the grid area at the time of the 1995 OASIS experiment. The four ground-based sites were located in crop or pasture fields and no ground-based sites were established over fallow fields. The *NDVI* image shows that these comprised approximately 10% of the land use at the time. The overlaid  $\overline{f^y}$  lines show that the aircraft sampled these areas and as a result, the fluxes measured by the aircraft will be more representative of the grid area.

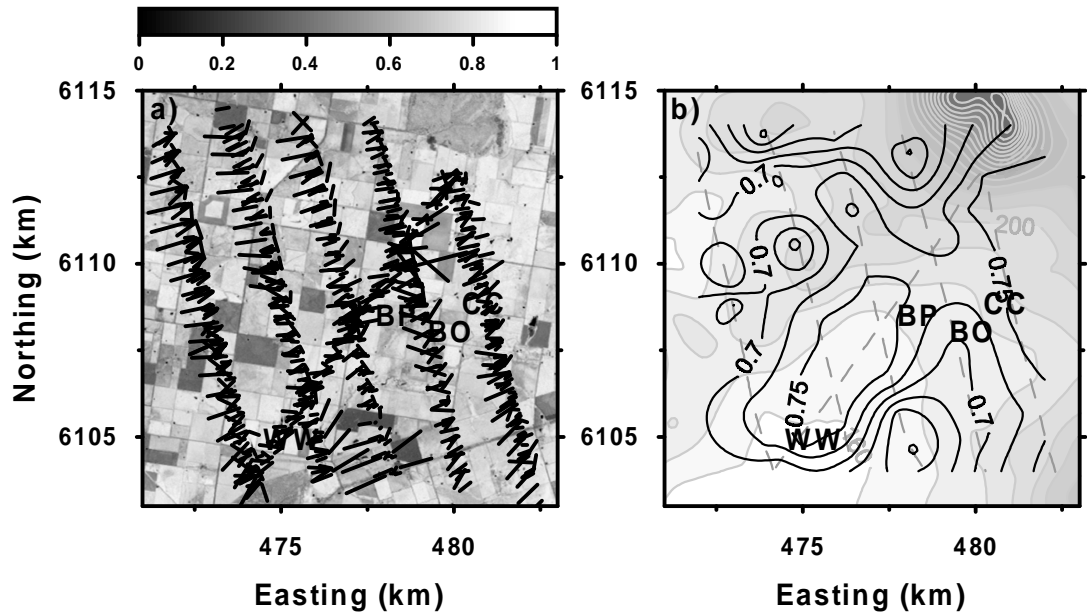


**Figure 6.7** a) *NDVI* image of the grid area with lines indicating the extent of the upwind area contributing 80% of the flux and b) contours of source-area weighted *NDVI* overlaid on the terrain of the grid area. Symbols BO, BP, CC and WW mark the Browning oats, Browning pasture, Cooinda canola and Wattles wheat sites respectively.

The contour plot of source-area weighted *NDVI* in Figure 6.7b shows similar features to the contour plots of  $\alpha_E$ ,  $\beta$ ,  $g_{sx}$  and  $W_{UE}$  for the grid area, see Figure 5.6 in Chapter 5. Maximum values of *NDVI* occur in the southwest corner and minima occur in the northwest and southeast corners. The same patterns are seen in the maxima and minima of the surface properties.

### 6.4.3 Aircraft Transect

Figure 6.8a shows the *NDVI* image of the OASIS domain overlaid with the crosswind integrated source-area weight for the aircraft transect flights and Figure 6.8b shows the source-area weighted *NDVI* for the ground-based and aircraft data.

The aircraft transect covered most of the gradient in *NDVI* across the OASIS domain. The significant land uses not covered were the unimproved pasture and sparse scrub at the western edge of the domain, areas of remnant native vegetation at various places across the whole domain and the agricultural lands in the northeast corner. The unimproved pasture, scrub and native vegetation have *NDVI* values of less than 0.53, the lowest value found for the ground-based sites. The agricultural

## Chapter Six

land in the northeast corner has  $NDVI$  values greater than 0.86, the highest value found for the ground-based sites. Combined, these land uses correspond to 20% of the area covered by the  $NDVI$  image. Using  $NDVI$  as a surrogate for the fluxes, evidence for which is presented later in this chapter, these results show that the ground-based and aircraft data are representative of 80% of the OASIS domain.

The source-area weighted  $NDVI$  shows a general increase from the dry, western end of the OASIS transect (Urana) to the wetter, eastern end (Wagga). The aircraft data shows significant variability in  $NDVI$  between the ground-based sites. At Urana and Browning, the  $NDVI$  values for the aircraft transect fall mid-way between those for the crop and pasture sites and this suggests that these ground-based sites are representative of their immediate surroundings. However, the  $NDVI$  values for the Wagga crop and pasture sites are greater than the values for the aircraft transect at this point. This is consistent with the comparison of aircraft and ground-based data presented in Chapter Four, which showed that ground-based observations  $F_E$  and  $F_C$  at Wagga were larger in magnitude than values from the aircraft data.

The overall variation of  $NDVI$  along the OASIS transect matches closely the variation in  $\alpha_E$ ,  $\beta$ ,  $g_{sx}$  and  $W_{UE}$  shown in Chapter Five (Figure 5.7). This suggests that the relationships between  $NDVI$  and the surface properties may be sufficiently strong to allow interpolation of these quantities from point measurements to regional scales. The relationships between the source-area weighted  $NDVI$  and the surface properties are examined in the following section.

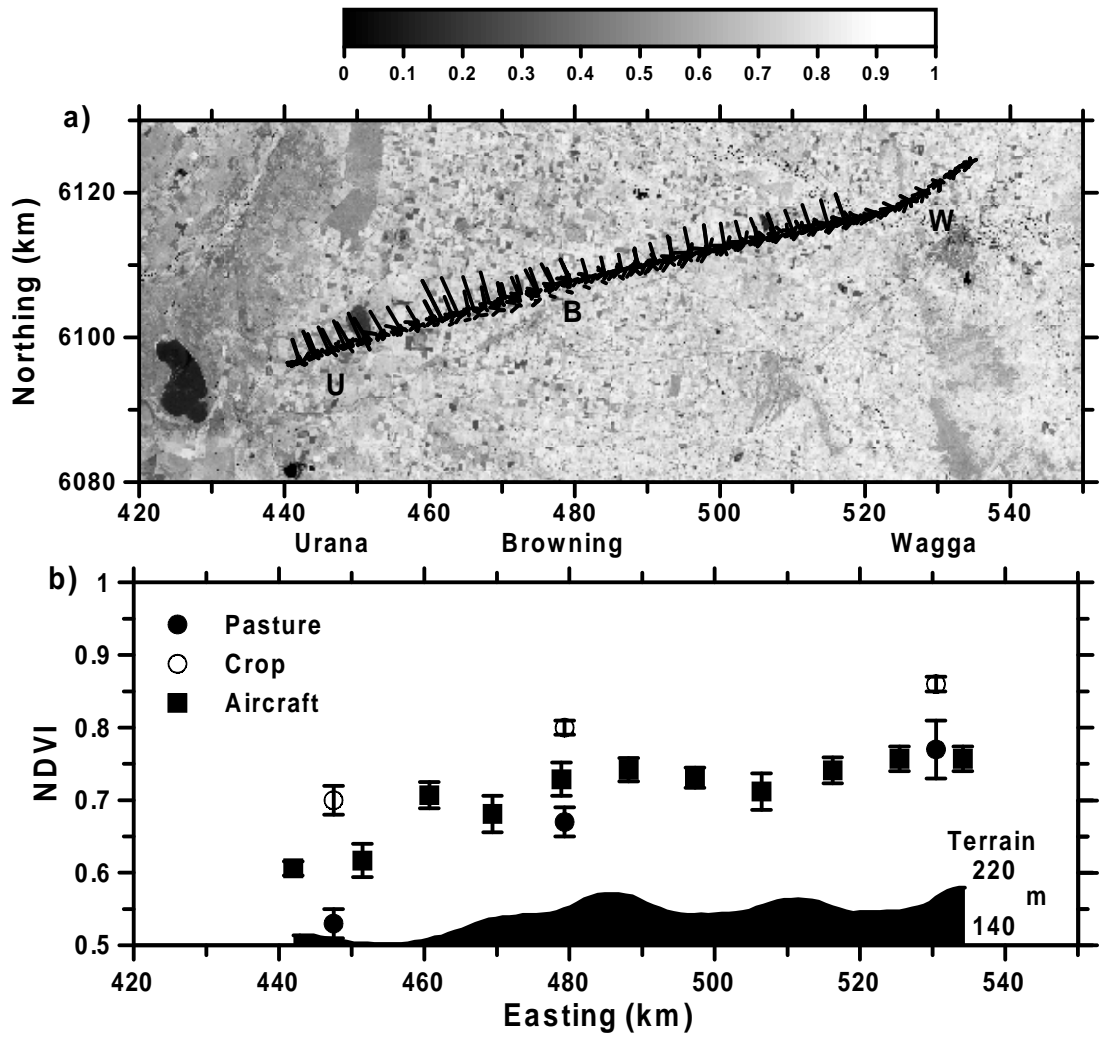


**Figure 6.8** a) *NDVI* image of the aircraft transect and b) plot of source-area weighted *NDVI* for the ground-based and aircraft data. The lines in the *NDVI* image indicate the extent of the upwind area contributing 80% to the aircraft flux observations. Symbols W, B and U are plotted directly below the Wagga, Browning and Urana sites, the true locations lie under the aircraft track. The error bars in the *NDVI* plot are plus and minus one standard deviation about the mean.

## 6.5 Surface Properties and *NDVI*

### 6.5.1 Ground-based Sites

Average values for the surface properties at the ground-based sites were given in Table 5.1 of Chapter Five. Figure 6.9 shows these plotted against the source-area weighted *NDVI*. The error bars in Figure 6.9 are plus and minus one standard deviation about the mean and the grey line is the line of best fit, the statistics for which are given in Table 6.3. The values of unity for  $r^2$  and zero for the confidence limits in the results for  $W_{UE}$  are due to the fact that there are only two points, Wagga and Browning, in the regressions. The outlying point in the plots of  $\alpha_E$ ,  $g_{sx}$  and  $\beta$  for the crop data comes from the wheat field at the Wattles site. The wheat field at this site reached maturity early in the 1995 OASIS experiment programme and, in addition, was damaged by heavy, local rainfall on 21 and 22 October 1995 (J. McAneney, pers. comm.). These two factors mean that the *NDVI* recorded on 8 October 1995 was not representative of the state of the crop during the latter half of the 1995 OASIS experiment. Data from the Wattles site has been excluded from the regression statistics for this reason.

**Table 6.3** Statistics for the lines of best fit in Figure 6.9,  $m$  is the slope,  $b$  is the intercept and  $r^2$  is the correlation coefficient squared. The uncertainties in  $m$  and  $b$  are the 90% confidence limits.

		$m$	$b$	$r^2$
$\alpha_E$	Crop	$2.4 \pm 0.9$	$-1.3 \pm 0.8$	0.90
	Pasture	$1.6 \pm 0.2$	$-0.5 \pm 0.1$	0.99
$g_{sx}$	Crop	$67 \pm 35$	$-45 \pm 27$	0.87
	Pasture	$80 \pm 61$	$-43 \pm 40$	0.86
$\beta$	Crop	$-8 \pm 4$	$7 \pm 3$	0.86
	Pasture	$-6 \pm 2$	$5 \pm 1$	0.97
$W_{UE}$	Crop	$-50 \pm 0$	$34 \pm 0$	1.00
	Pasture	$-56 \pm 0$	$35 \pm 0$	1.00

The relationship between the source-area weighted *NDVI* and  $W_{UE}$  can not be tested using this data because there are only two points in the regression. The relationships between the source-area weighted *NDVI* and  $\alpha_E$ ,  $\beta$  and  $g_{sx}$  are approximated well

by linear fits with high correlation coefficients of between 0.86 and 0.99 but the 90% confidence limits for the slope and intercept are relatively large.

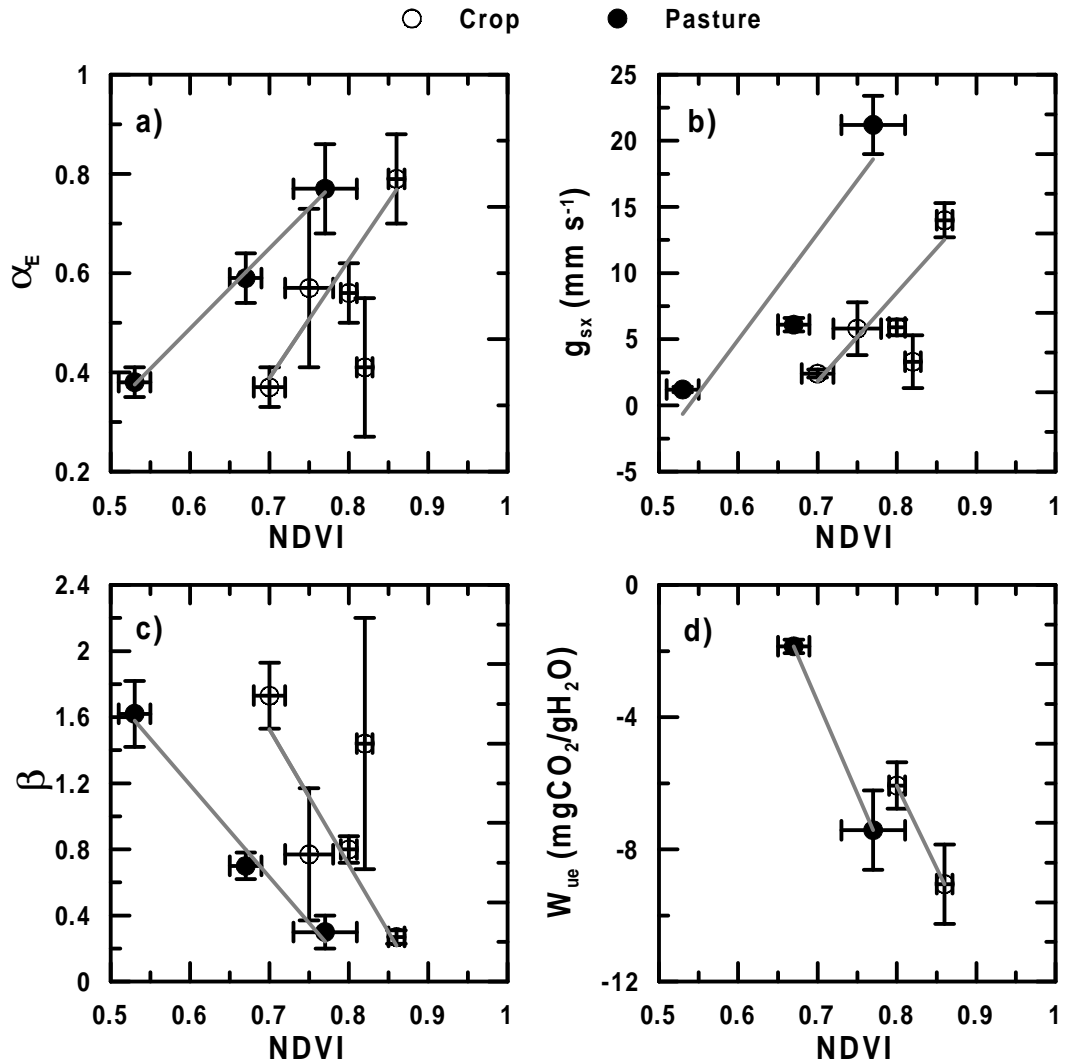


**Figure 6.9** Plots of a)  $\alpha_E$ , b)  $g_{sx}$ , c)  $\beta$  and d)  $W_{UE}$  as functions of the average source-area weighted  $NDVI$  for the ground-based sites. The solid grey line is the line of best fit with statistics given in Table 6.3.

The results show that the relationship between the surface properties and  $NDVI$  is different for the crop and pasture sites during the 1995 OASIS experiment. This is because, with the exception of  $W_{UE}$ , there is no consistent difference between the surface properties for the paired crop and pasture fields (Table 5.1) but  $NDVI$  does differ significantly between these land uses (Table 6.2). In other words,  $\alpha_E$ ,  $g_{sx}$  and  $\beta$  do not discriminate against crop or pasture but  $NDVI$  does and this leads to

ambiguous relationships between  $NDVI$  and these surface properties. For example, the same value of  $NDVI$  is associated with different values of  $\alpha_E$ , or  $g_{sx}$  or  $\beta$ , occurring at different locations along the transect. This means that  $NDVI$  alone is not sufficient to accurately predict these quantities for crop and pasture individually over the OASIS domain. Additional information is required.

In the case of the 1995 OASIS experiment, the additional information could be supplied by antecedent rainfall since this varies smoothly from Urana to Wagga. Antecedent rainfall combined with  $NDVI$  would then provide sufficient information to be able to discriminate between crop and pasture at any location along the transect, leading to accurate predictions of the surface properties for each land use. However, an alternative approach is adopted here that is in keeping with the goals of simplicity and integration of aircraft and ground-based data.

Aircraft data must be averaged over sufficient distance to produce stable estimates of the turbulent fluxes. The averaging length of 10 km used for the OASIS transect flights is much larger than the typical field dimensions and this means that the aircraft data averages the contributions from adjacent crop and pasture fields. In other words, the aircraft data, as used here, can not discriminate between crop and pasture either and so it is appropriate to average the ground-based data from paired crop and pasture sites at each location along the transect. Averaging the ground-based data yields quantities that are directly comparable with those from the aircraft and allows the ground-based and aircraft data to be integrated in order to examine the relationship between  $NDVI$  and the surface properties. The use of average crop and pasture data to define the relationships is equivalent to ignoring microscale heterogeneity and only using  $NDVI$  to resolve mesoscale and macroscale heterogeneity. The OASIS results demonstrate that the variability in the fluxes at the microscale is much less than the variability at the macroscale and ignoring the microscale will have little effect on the estimation of regional scale fluxes.

### 6.5.2 Synthesis of Ground-based and Aircraft Data

Figure 6.10 shows the relationships between  $NDVI$  and the surface parameters,  $\alpha_E$ ,  $g_{sx}$ ,  $\beta$  and  $W_{UE}$  for the ground-based and aircraft data. The ground-based data are

averages of the paired crop and pasture sites, calculated using the methods described in Chapter Five. The statistics for the lines of best fit are given in Table 6.4.

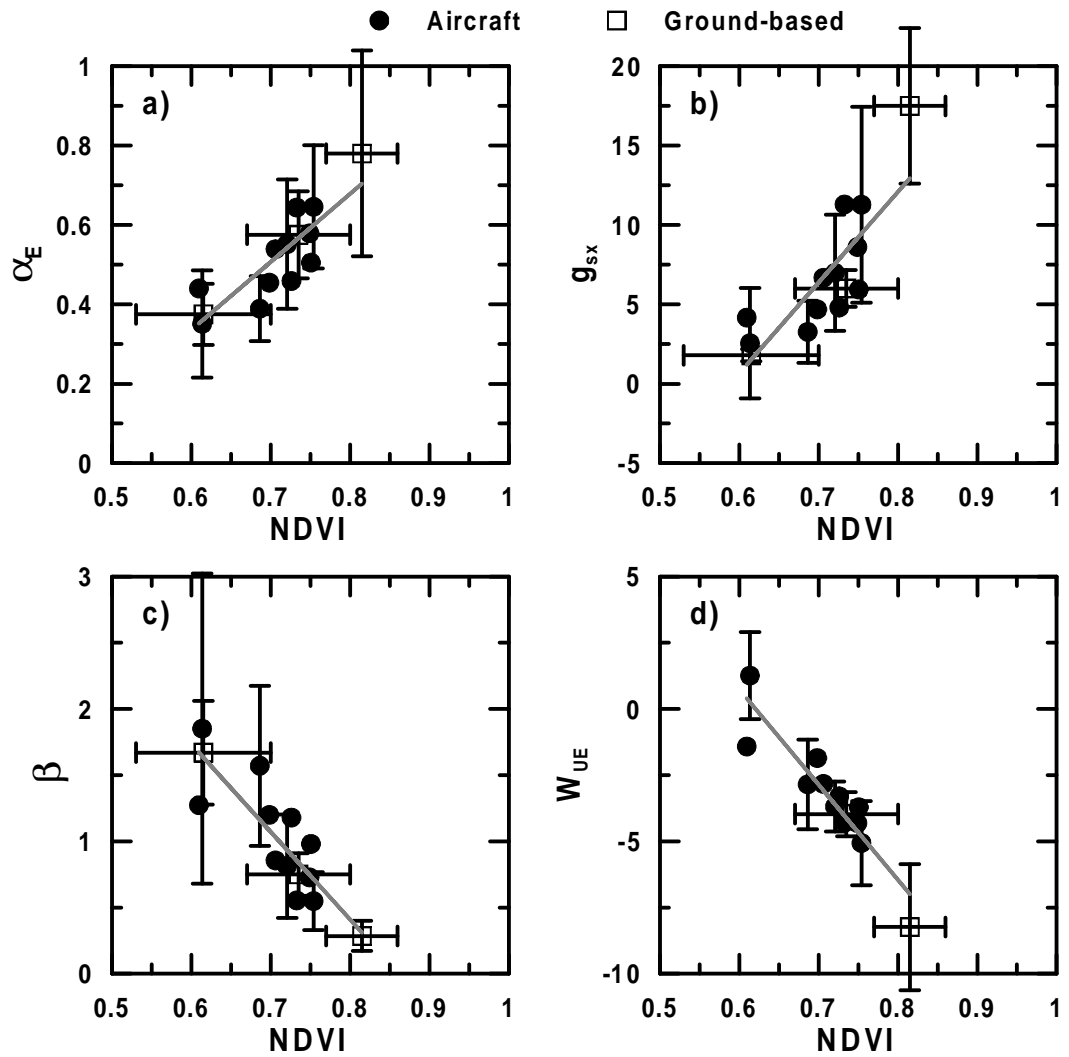


**Figure 6.10** Plot of a)  $\alpha_E$ , b)  $g_{sx}$ , c)  $\beta$  and d)  $W_{UE}$  versus source-area weighted  $NDVI$  along the aircraft transect (solid) and for the ground-based (open) sites. The grey line is the line of best fit. Vertical error bars are plus and minus one standard deviation and are only plotted on every third aircraft data point for clarity. Horizontal error bars are plotted for the ground-based data only and show the range in  $NDVI$  between crop and pasture.

**Table 6.4** Statistics for the lines of best fit in Figure 6.10,  $m$  is the slope,  $b$  is the intercept and  $r^2$  is the correlation coefficient squared. The uncertainties in  $m$  and  $b$  are the 90% confidence limits.

	$m$	$b$	$r^2$
$\alpha_E$	$1.7 \pm 0.6$	$-0.7 \pm 0.4$	0.73
$g_{sx}$	$57 \pm 34$	$-34 \pm 16$	0.66
$\beta$	$-6 \pm 2$	$6 \pm 1$	0.75
$W_{UE}$	$-36 \pm 9$	$22 \pm 6$	0.85

Figure 6.10 and Table 6.4 show that the relationships between  $NDVI$  and the surface properties are well described by a linear dependence over the range of  $NDVI$  encountered. However, the slope and intercept values in Table 6.4 suggest that these relationships can not be linear over a wider range of  $NDVI$  values. For example, the relationship between  $NDVI$  and  $\alpha_E$  implies a negative value of  $\alpha_E$  when the  $NDVI$  drops below 0.4. The  $NDVI$  values for fallow fields in Figure 6.7a drops to 0.25 and evaporation from these surfaces is likely to be close to zero once the top few centimetres of soil have dried out after rain. This means that the evaporative fraction should approach zero as  $NDVI$  approaches the value for bare soil and not assume negative values as implied by the relationship in Table 6.4. Similar arguments can be made in the case of  $g_{sx}$ ,  $\beta$  and  $W_{UE}$ . These results emphasise the fact that the empirical relationships between the surface properties and  $NDVI$  can not be applied outside the range of  $NDVI$  for which they were derived.

In the plots of  $\alpha_E$ ,  $g_{sx}$  and  $W_{UE}$ , the points for the ground-based sites at Browning and Urana lie in the midst of the aircraft data whereas the points for Wagga all have larger magnitudes than suggested by the line of best fit. As noted in Section 6.4.3, the source-area weighted  $NDVI$  for a 10 km segment that passed within 1 km of the Wagga site was 0.75 compared to an average value of 0.82 for the Wagga crop and pasture fields. These results show that the Wagga site was significantly different from the surface sampled by the aircraft in its closest approach to the tower. The sensitivity of the regression statistics to the values at Wagga was checked by excluding these data points from the analysis, this did not significantly alter the values for  $m$  and  $b$  but the values of  $r^2$  were somewhat reduced.

The correlation coefficients in Table 6.4 are high and in most cases, the 90% confidence interval is less than half of the value for the slope or intercept. This means that the relationships are robust and can be used to interpolate the observations of the surface properties over the OASIS domain provided they are not applied outside the *NDVI* range from which they were derived. This process is described in the following section.

### 6.5.3 Extension of Point Observations to OASIS Domain

The relationships between *NDVI* and the surface properties listed in the previous section can be used to interpolate values between the ground-based sites along the transect. In addition to this, much of the area covered by the Landsat image is characterised by the same agricultural land use with *NDVI* values within the range used to define the relationships. This allows the relationships to be used to interpolate the point measurements over approximately 80% of the area covered by the Landsat image.

Figure 6.11 shows contour plots of  $\alpha_E$ ,  $g_{sx}$ ,  $\beta$  and  $W_{UE}$  for the OASIS domain overlaid on the *NDVI* image. The *NDVI* values have been averaged over 5 km by 5 km squares before calculating the surface properties. This was done to display the main features without the distraction of detail caused by microscale heterogeneity that is not resolved by *NDVI* alone, see Section 6.5.1. Contours have not been plotted for *NDVI* values outside the range used in Section 6.5.2 to define the relationship between *NDVI* and the surface properties.

All of the contour plots show similar patterns because the surface properties are modelled as linear functions of *NDVI*. The obvious feature in all plots is the west to east trend driven by the rainfall gradient. Superimposed on this trend are several smaller scale features indicating areas of enhanced or suppressed water vapour and CO<sub>2</sub> fluxes. The reasons for this mesoscale heterogeneity can not be conclusively demonstrated because of the limited ground-based data but the most likely reason is variability in the soil moisture driven by local drainage patterns, soil type and rain shadows.

## Chapter Six

A comparison of the surface property values at the ground-based sites with the patterns evident in Figure 6.11 helps to place the ground-based sites in the context of their surroundings. The values for the Urana and Browning sites are in general agreement with the contour plots but the values of  $\alpha_E$ ,  $g_{sx}$  and  $W_{UE}$  at Wagga are consistently larger in magnitude than those suggested for this site on the basis of the *NDVI* image. This reflects the fact that the points for Wagga all lie to one side of the regression lines shown in Figure 6.10 and serves to emphasise that the Wagga site was not representative of its immediate surroundings.

Several of the smaller scale features are associated with surface types that are not represented in the data used to derive the relationships between *NDVI* and the surface properties and care is required when interpreting these results. Examples of this are the pockets of remnant native vegetation located at 509 km Easting, 6092 km Northing and 535 km Easting, 6080 km Northing, the urban area of Wagga Wagga at 532 km Easting, 6113 km Northing. No measurements were made over these surfaces during the 1995 OASIS experiment and the expressions in Section 6.5.2 can not be applied. These areas, combined with the arid western extremity of the Landsat image, comprise approximately 20% of the total area and have been excluded from further analysis.

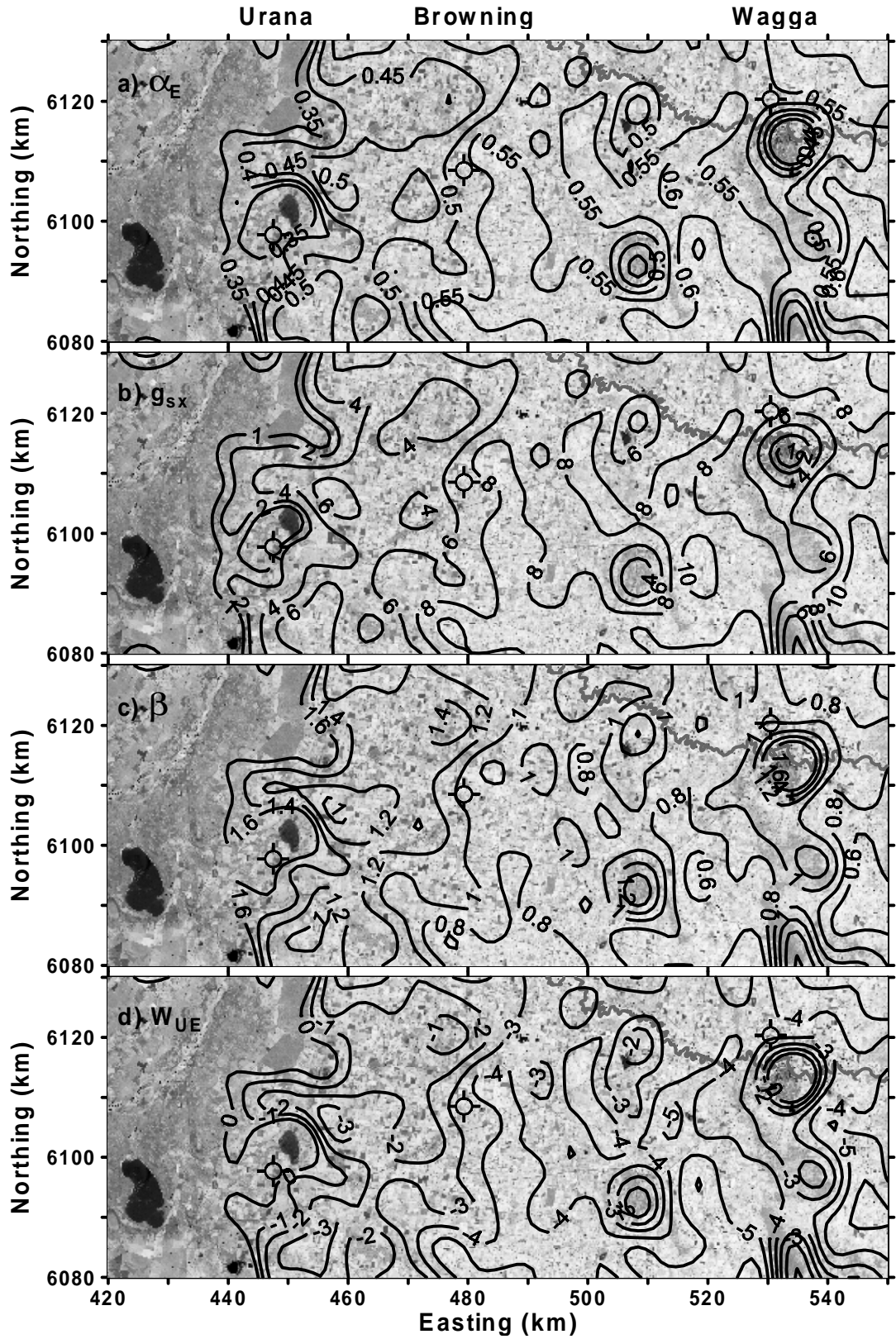


**Figure 6.11** Contour plots of a)  $\alpha_E$ , b)  $g_{sx}$ , c)  $\beta$  and e)  $W_{UE}$  derived from *NDVI* for the OASIS domain.

## 6.6 Summary and Conclusions

Remotely sensed data provide a practical means for assessing regional and global scale variations in land use but there is currently no theoretical framework that directly relates remotely sensed quantities to surface properties. Until such a framework exists, the only option is to derive empirical relationships based on coincident satellite images and in-situ observations of micrometeorological quantities. The in-situ observations can come from ground-based towers or from aircraft but whichever method is used, a model for estimating the source-area is required to relate the observations to the surface patch contributing the majority of the measured flux. The source-area model then provides the link between the observations, the surface and the remotely sensed data, allowing the relationship between the observations and the remotely sensed data to be examined.

A model based on an approximate analytical solution to the advection-diffusion equation has been used in this study because it combines good accuracy with low computational overhead. The source-area weight function given by this model was applied to an *NDVI* image of the OASIS domain to estimate the source-area weighted *NDVI* of the surface patches influencing the ground-based and aircraft observations. The major limitations of this method are the assumptions required in obtaining an analytic solution to the advection-diffusion equation and the restriction to observations within the surface layer. The latter point is the most serious when dealing with aircraft observations since it restricts the aircraft operations to low altitudes of 20 to 30 m in daytime, unstable conditions.

Plotting the upwind extent of the surface contributing 80% of the measured flux allows the fetch of the ground-based sites to be assessed. This shows that the upwind fetch for the Wagga triticale and pasture, Browning oats and Urana wheat sites often extended beyond the fields containing the instruments. However, the source-area weight function peaks close to the measurement location and drops off rapidly with increasing upwind distance. This means that the contribution from the adjacent fields will be small. Fetch requirements are usually decided by "rule of thumb" but the source-area method allows the validity of this approach to be assessed and offers

the possibility of using the source-area as a criterion for data quality control during processing.

The combination of the source-area model and a satellite image allows the surface patch influencing the observations to be positively identified. This is a significant advance over the practice of relying on aircraft-based observations of *NDVI* (Mahrt et al., 1998) since surface conditions in the field of view beneath the aircraft may not match those of the upwind patch contributing to the flux. The greatest benefit with this technique is obtained at low aircraft altitudes (<30 m) and with high resolution images (pixel size 25 m). The upwind extent of the source-area weight function expands rapidly as the measurement height increases and this will tend to obscure small surface features. The same is true for pixel sizes of 1 km, such as available from the MODIS or AVHRR sensors, because small-scale features will be obscured by the averaging within the pixel.

Aircraft and ground-based data were used to explore the connection between the surface properties and the source-area weighted *NDVI*. The averaging length for the aircraft data was 10 km, larger than the typical field dimensions, which means that the aircraft data at any point along the transect are averages of conditions over both crop and pasture fields. To simulate this, and because *NDVI* alone is not enough to discriminate between crop and pasture, the ground-based data for paired crop and pasture sites were averaged. The relationships between *NDVI* and the aircraft and averaged ground-based data are well represented by linear expressions for the range of conditions encountered during the 1995 OASIS experiment.

The relationship between *NDVI* and the surface properties can be used to assess the degree to which the surface contributing to a measurement is representative of a wider area. This is important when comparisons are made between ground-based and aircraft observations because even small differences in adjacent fields of the same land use may lead to bias in the comparison (Isaac et al, 2004a). Relating aircraft and ground-based measurements to the *NDVI* of the surface demonstrates that the source-areas of the ground-based observations at Urana and Browning were representative of the surface sampled by the aircraft. This was not the case at Wagga

## Chapter Six

where the source-area weighted *NDVI* of the aircraft measurements is substantially less than the value for the ground-based observations.

The relationships between the surface properties and *NDVI* allow the aircraft and ground-based measurements of these quantities to be interpolated over a 130 km by 50 km area with the same land use as the OASIS transect. The relationships are empirical and their use is restricted to the conditions under which they were derived unless their generality can be demonstrated by further work. However, the ability to extend such observations to large regions is significant because it raises the possibility of using remotely sensed data to provide inputs to models of biosphere-atmosphere interactions. This use is tested in the following chapter.

## 6.7 Appendix: Source-area Model

### 6.7.1 Equation Set

The source-area weight function can be written as (Horst and Weil, 1992):

$$f(x, y, z_m) = D_y(x, y) \bar{f}^y(x, z_m), \quad 6.6$$

where  $f(x, y, z_m)$ , the source-area weight, is the fractional contribution of an elemental surface area located at  $(x, y, 0)$  to an observation made at  $(0, 0, z_m)$ .

$D_y(x, y)$  is the crosswind distribution function and  $\bar{f}^y(x, z_m)$  is the crosswind integrated (CWI) source-area weight function.

The crosswind distribution function is taken to be Gaussian (Horst and Weil, 1992):

$$D_y(x, y) = \frac{1}{\sqrt{2\pi}\sigma_y} \exp(-y^2/2\sigma_y^2), \quad 6.7$$

where  $y$  is the crosswind displacement and the horizontal plume spread,  $\sigma_y$ , is a function of lateral turbulence intensity and upwind distance. It can be calculated using (Pasquill, 1976):

$$\sigma_y = \frac{\sigma_{wD}x}{(1 + 0.0208\sqrt{x})}, \quad 6.8$$

where  $\sigma_{wD}$  is the standard deviation of the wind direction and  $x$  is the upwind distance.

An expression that relates the crosswind integrated source-area weight function,  $\bar{f}^y$ , to the crosswind integrated concentration distribution,  $\bar{C}^y$ , can be obtained by integrating the 2-dimensional advection-diffusion equation from the surface to the measurement height (Horst and Weil, 1992):

$$\bar{f}^y = -\int_0^{z_m} \bar{u}(z) \frac{\partial}{\partial x} \bar{C}^y(x, z) dz, \quad 6.9$$

where  $\bar{u}(z)$  is the mean wind speed profile. The crosswind integrated concentration distribution is assumed to be of the form (Horst and Weil, 1992):

$$\bar{C}^y(x, z) = \frac{A}{U(x) \bar{z}(x)} \exp\left(-\left(z/b\bar{z}(x)\right)^r\right), \quad 6.10$$

where:

$$A = r\Gamma(2/r)/\Gamma^2(1/r) \text{ and } b = \Gamma(1/r)/\Gamma(2/r) \quad 6.11$$

and  $\Gamma$  is the gamma function. The remaining terms in Equation 6.10 are  $\bar{z}(x)$ , the mean, concentration-weighted plume height as a function of upwind distance,  $U(x)$ , the mean, concentration-weighted plume advection velocity and  $r$ , the shape of the vertical concentration profile. These quantities are discussed in the following paragraphs.

van Ulden (1978) gives an expression for  $\bar{z}$  in the form of a differential equation but this must be solved numerically to give  $\bar{z}$  values as a function of upwind distance. Horst and Weil (1994) integrate this differential equation to give an equivalent expression for calculating upwind distance  $x$  as a function of  $\bar{z}$ :

$$\frac{x}{z_0} = \int_{z_0}^{\bar{z}(x)} \left(\frac{\partial \bar{z}'}{\partial x}\right)^{-1} d\bar{z}' \equiv \Psi(\bar{z}) - \Psi(z_0), \quad 6.12$$

where  $z_0$  is the roughness length for momentum. Horst and Weil (1995) give the following expression for  $\Psi(\bar{z})$  in unstable conditions:

$$\Psi(\bar{z}) = \frac{1}{k^2} \frac{2|L|}{\gamma p z_0} \left\{ y_p^2 \left[ \ln\left(\frac{p\bar{z}}{z_0}\right) - \psi_m(y_p) \right] + 2 \tan^{-1}(y_p) + \ln\left(\frac{y_p+1}{y_p-1}\right) - 4y_p \right\}, \quad 6.13$$

$$y_p \equiv \left(1 - \frac{\gamma p \bar{z}}{L}\right)^{1/4}$$

where  $k = 0.4$  is the von Karman constant,  $\gamma = 16$  and  $L$  is the Monin-Obukhov length. van Ulden (1978) gives an expression for  $p$  as a function of the shape

## Relating Surface-atmosphere Exchange to Remotely Sensed Quantities

parameter  $r$  but points out that  $p$  is insensitive to the exact value of  $r$  and to a good approximation can be taken as  $p \approx 1.55$ .

$\psi_m$  in Equation 6.13 is the diabatic correction to the logarithmic wind profile and is given by:

$$\psi_m = 2 \ln \left( \frac{y+1}{2} \right) + \ln \left( \frac{y^2+1}{2} \right) + 2 \tan^{-1} \left( \frac{1-y}{1+y} \right),$$

$$y = \left( 1 - \frac{\gamma z}{L} \right)^{1/4}.$$
6.14

Details of the implementation of Equation 6.12 are given in Section 6.7.2.

$U(x)$  is the mean (concentration weighted) plume advection velocity and an approximate expression for the equivalent quantity  $U(\bar{z})$  in unstable conditions is given by van Ulden (1978):

$$U(\bar{z}) \approx \frac{u_*}{k} \left[ \ln \left( \frac{c\bar{z}}{z_0} \right) - \psi_m \left( \frac{c\bar{z}}{L} \right) \right],$$
6.15

where a value of 0.63 has been assumed for  $c$ . Horst and Weil (1994) give an expression for calculating  $c$  but this requires a value for  $r$ , which is itself dependent on  $c$ . A constant value for  $c$  was chosen to avoid this circularity.

The last parameter in Equation 6.10 is the shape parameter,  $r$ . This parameter describes the shape of the vertical concentration distribution of a passive scalar diffusing from a point source at the surface. A value of  $r=1$  gives an exponential distribution, approached in unstable conditions, and a value of  $r=2$ , gives a Gaussian distribution which is approached in moderately stable conditions (Horst and Weil, 1992). Gryning et al. (1983) give a set of empirical relations for  $r$  as a function of  $\bar{z}$ ,  $z_0$  and  $L$  that are based on fitting Equation 6.10 to numerical solutions of the advection-diffusion equation. Kaharabata et al. (1997) derive a single value for  $r$  for use over a forest canopy in near-neutral conditions from gas tracer experiments conducted during BOREAS. The value of  $r$  has recently been the subject of an interesting discussion in the literature, see Haenel and Grunhage (1999), the comment from Horst (2001) and the subsequent reply from Haenel and

Grunhage (2001). The empirical relations for  $r$  given in Gryning et al. (1983) have been used in the current work on the basis that these relations have been tested against experimental data by Finn et al. (1996). The expression for unstable conditions is:

$$r = \frac{1 - 4.5c\bar{z}/L}{1 - 9c\bar{z}/L} + \frac{(1 - 15c\bar{z}/L)^{-1/4}}{\ln(c\bar{z}/z_0) - \psi_m(c\bar{z}/L)}. \quad 6.16$$

Equation 6.9 can not be solved analytically when Monin-Obukhov similarity profiles are used for the mean wind speed and eddy diffusivity. Horst and Weil (1994) suggest the following approximate solution:

$$\bar{f}^y(x, z_m) \approx \frac{d\bar{z}}{dx} \frac{z_m}{\bar{z}^2} \frac{\bar{u}(z_m)}{U(\bar{z})} A \exp\left(-\left(z_m/b\bar{z}\right)^r\right) \quad 6.17$$

The authors state that the error in this approximation is a 5% overestimation for unstable conditions with a similar magnitude underestimation in stable conditions. These errors are small in the context of the current application and are tolerated in exchange for the computational efficiency of Equation 6.17. The overall accuracy of this approximation can be assessed by checking that the cumulative sum of  $\bar{f}^y$  approaches unity at large upwind distances. The implementation of Equation 6.17 used in this work has been checked over the range  $-1 \leq z/L \leq 2$  and the cumulative sum of  $\bar{f}^y$  remained within  $\pm 5\%$  of 1.00. This is considered an acceptable level of error (Horst, 1999).

### 6.7.2 Numerical Method

Equations 6.17, 6.7 and 6.6 provide a method for calculating the three-dimensional source-area weight function. No detailed description of the necessary steps was found in the literature and the procedure adopted here is described in the following paragraphs. Necessary inputs are the measurement height  $z_m$ , the momentum roughness length  $z_0$ , the Monin-Obukhov length  $L$ , the standard deviation of wind direction  $\sigma_{WD}$  and the friction velocity  $u_*$ .

## Relating Surface-atmosphere Exchange to Remotely Sensed Quantities

The numerical method begins with calculation of  $x(\bar{z})$  at regularly spaced values of  $\bar{z}$  using Equation 6.12. Values of  $\bar{z}$  at intermediate upwind distances are obtained by linear interpolation as required. This method is much faster than numerical integration of the expression for  $d\bar{z}/dx$  in van Ulden (1978) however this expression is used to calculate  $d\bar{z}/dx$  for Equation 6.17. Once  $\bar{z}(x)$  has been determined,  $U(\bar{z})$  can be calculated using Equation 6.15, followed by  $r$ ,  $A$  and  $b$  using Equations 6.16 and 6.11 respectively. Equation 6.8 is then used to calculate  $\sigma_y$  and the mean wind speed at  $\bar{z}$  calculated from the logarithmic profile corrected for stability.

Next, the maximum value of the source-area weight function  $f(x, y, z_m)$  is found using a numerical search routine and the integral of  $f(x, y, z_m)$  calculated for 19 fractional values (range 0.001 to 0.975) of this maximum. These integrals represent the fractional contribution to the observed flux at the  $f(x, y, z_m)$  values used. However in order to calculate the source-area, it is necessary to know the value of  $f(x, y, z_m)$  that corresponds to a specific fractional (10%, 20% etc) contribution to the observed flux. Schmid (1994) claims to fit a function to the set of points given by the fractional values of  $f(x, y, z_m)$  and their corresponding contributions and to use this function to calculate the source-area weight value for a given contribution. A number of functions were tried in this work but none were found that gave an adequate fit to the points for a suitable range of measurement heights and stabilities. Linear interpolation to the desired contribution between the fractional values of  $f(x, y, z_m)$  was used after inspection of the points showed them to be smoothly varying. The isopleth of the source-area contributing a given percentage to the flux can be calculated once the  $f(x, y, z_m)$  values bounding this contribution have been found.

The approximate analytical form for  $\bar{f}^y$  given in Equation 6.17 allows Equation 6.6 to be inverted to give an expression for the crosswind distance ( $y$ ) as a function of the upwind distance ( $x$ ) and value of  $f(x, y, z_m)$ . This means that the  $y$  limits

required to integrate Equation 6.6 in two dimensions can be calculated explicitly provided the integration is performed in the  $dydx$  order. This is opposite to the  $dx dy$  order used in Schmid (1994) which requires a second curve fit procedure to provide the relationship between the  $x$  and  $y$  limits of the integration. The use of the explicit method, and the linear interpolation to get values of  $f(x, y, z_m)$  at 10%, 20% etc contribution to the flux, significantly improves both the speed and the accuracy of the source-area calculations.

The procedure outlined above was implemented in the Interactive Data Language (IDL, Research Systems Incorporated, Boulder, USA) using numerical methods described by Press et al. (1992). The implementation was checked by calculating the integral of  $f(x, y, z_m)$  to 0.01% of the maximum value for a range of measurement heights, stabilities and roughness lengths. The integral remained within  $1.00 \pm 0.05$  for all cases. As a further check, the values of  $\overline{f}^y$  were compared to those given in Figure 2 of Horst (1999) and no differences were found.

### 6.7.3 Source-area Example

Examples of the three-dimensional source-area weight functions for measurement heights of 4.5 and 20 m are shown in Figure 6.12. The solution is for unstable conditions typical of the aircraft flights during the 1995 OASIS experiment with  $L = -30$  m,  $u_* = 0.3$  m s<sup>-1</sup>,  $z_0 = 0.03$  m and  $\sigma_{wD} = 20^\circ$ . The plot for 4.5 m is stacked directly above the plot for 20 m and the crosswind and upwind axes scaling are the same for both plots. The surfaces are shaded from black at the maximum value of the source-area weight function to mid-grey and have been truncated at 1% of the maximum value. Integrals over the surfaces to the 0.01% isopleths are 1.03 and 1.01 for 4.5 and 20 m respectively.

The plots show the differences between the source areas contributing to the ground-based observations at 4.5 m and the aircraft observations at 20 m. The source-area weight function for the ground-based observations is very narrow and sharply peaked compared to that for the aircraft observations. The maximum value of  $f(x, y, z_m)$  for the ground-based data is approximately four times larger than for the aircraft data

and the upwind extent is approximately five times less. The results demonstrate the large difference between the surface areas influencing the aircraft and the ground-based measurements.

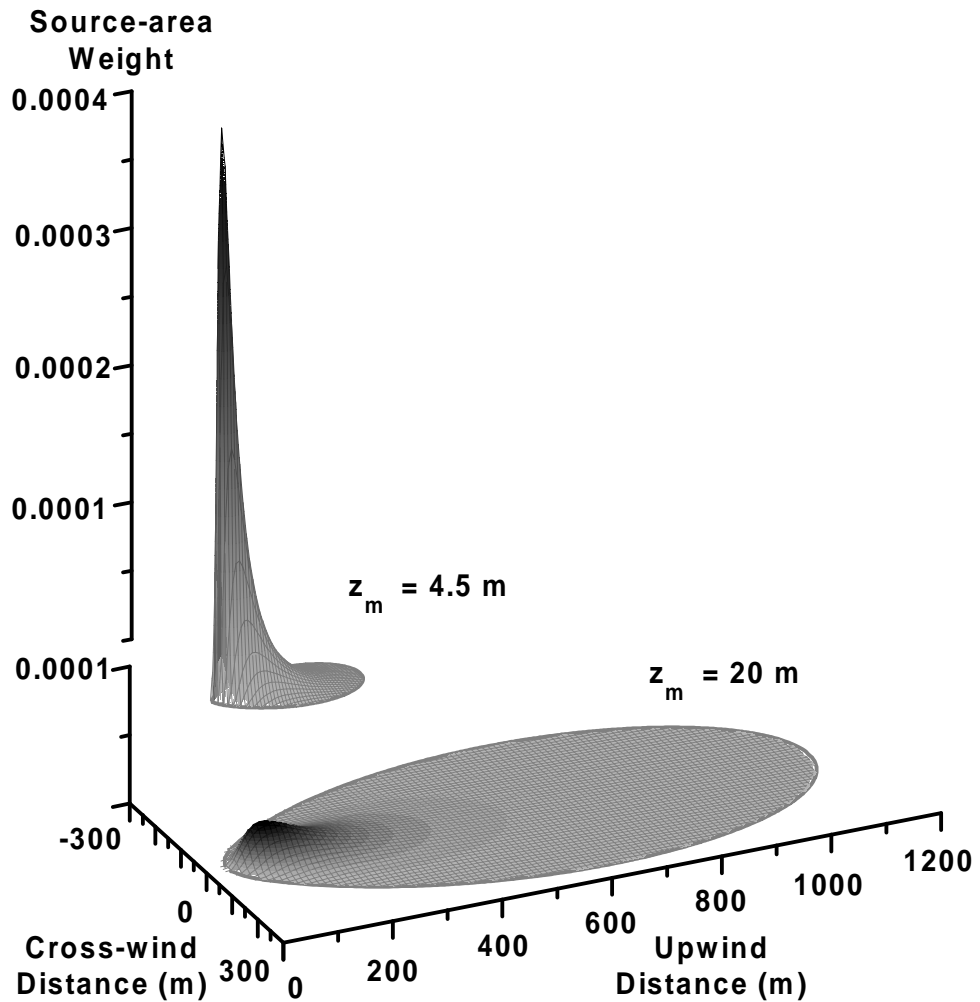


**Figure 6.12** Three-dimensional plots of the source-area weight function for measurement heights of 4.5 m (upper) and 20 m (lower).